International Journal of Enhanced Research in Science, Technology & Engineering
ISSN: 2319-7463, Vol. 12 Issue 6, June-2023, Impact Factor: 7.957

FSI deformation of NACA spoiler under airload calculated by using numerical solution and validate with laboratory test

Luigi Buffone

Department of Mechanical Engineering, Slovak University of Technology in Bratislava (STU), Bratislava, Slovak

ABSTRACT

The fluid-structure interaction (FSI) iteration arises from the deformation of the spoiler subjected to air loads, causing a variation in the initial surface and the aerodynamic forces that change when the airfoil profile flexes and/or twists. The altered structure gives rise to altered lift, pitch, and drag, depending on the amount of deformation of the spoiler itself. The numerical analysis is of a steady-state nature with one-way coupling, using the Fluent CFD module to calculate the loads, which are then transferred to the FEM module to obtain the deformations. The numerical analysis was conducted for various velocities, different angles of attack, for PLA materials constituting the spoiler in question. The aerodynamic characteristics of a three-dimensional asymmetric spoiler with a high downforce load have been studied, analyzed numerically, and subsequently validated in the laboratory.

Keywords: CFD, FEM, FSI, airfoil, spoiler deformaion, airload, lift, drag, pitch, bending, torsion, flexural

INTRODUCTION

The air striking the spoiler generates both fluid forces, which are related to the wind speed, profile design, airfoil surface, and angle of attack, as well as the deformation of the spoiler, which depends on the static air pressure, structural configuration of the spoiler, and material type. There are few available data in the literature regarding deformable aerodynamic profiles applied to cars for generating downforce, as the materials used for current spoilers are mainly aluminum or high-rigidity composite materials designed for the examined velocities. The numerical model was created using CAD and then shared with the CFD and FEM solvers for their respective simulations separately. The pressure calculated with CFD was transferred to FEM as an imported airload, from which the displacements and rotations of the points of interest were calculated.

Nomenclature

ρ air density	m mass of spoiler
t time	I Moment of Inertial
u velocity in x-direction	E Young's modulus
v velocity in y-direction	
w velocity in z-direction	
V velocity	
p air pressure	
ν air viscosity	

METHODOLOGY

The FSI (Fluid-Structure Interaction) problem was approached using a one-way coupling between the fluid and structure, where the interaction interface was represented by the surface of the spoiler. The fluid modeling was accomplished using Computational Fluid Dynamics (CFD), while the structural part was modeled using the Finite Element Method (FEM) with a non-penetration boundary condition. The 1-way FSI simulation was made possible by connecting the CFD and FEM modules, which worked alternately and it means that the results from CFD were transferred to FEM. The 1-way FSI simulation was made possible by connecting the CFD and FEM modules, which worked alternately and it means that the results from CFD were transferred to FEM.

However, it's important to note that the one-way coupling does not consider the effect of spoiler deformations on aerodynamic forces such as drag, lift, and pitch. The advantage of this coupling is that the same CFD results can be used to calculate new deformations. In the CFD module, the spoiler interface is treated as a rigid cavity with conditions such as no-slip, no-penetration boundary, and boundary. This surface is where the airload transfer occurs and represents the surfaces of the spoiler. In the FEM environment, the CFD domain is deactivated, and the airload is represented as an imported external pressure on the spoiler under a cantilever beam configuration.

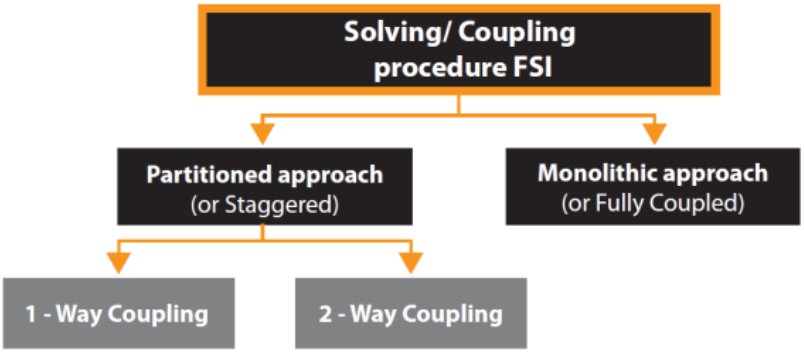

Figure 1: FSI Coupling Procedure

Type of Approach

The equations used for finite volume analysis are the continuity equation and the Navier-Stokes equations reported below: [5, 10]

$$\frac{\partial \rho}{\partial t}+\frac{\partial(\rho u)}{\partial x}+\frac{\partial(\rho v)}{\partial y}+\frac{\partial(\rho w)}{\partial z}=0 \tag{1}$$

$$\frac{\partial V_i}{\partial t}+V_i\frac{\partial V_i}{\partial x_j}=-\frac{1}{\rho}\frac{\partial p}{\partial x_i}+\nu\frac{\partial^2 V_i}{\partial x_i \partial x_j} \tag{2}$$

As for the deformations in finite element analysis, they follow the Euler-Bernoulli's beam equation [3]

$$\frac{\partial^2}{\partial x^2}\left(EI\frac{\partial^2 v}{\partial x^2}\right)+m\frac{\partial^2 v}{\partial t^2}=f(x,t) \tag{3}$$

The fluid domain is bounded by a surface that extends 3.5 times the chord of the spoiler in the front and 7 times the chord of the spoiler behind the structure and therefore its lengths are 350 cm and 700 cm, respectively. Additionally, the depth of the domain is 440 cm, [1] which is greater than the span of the spoiler (fig. 2). An asymmetric spoiler of the NACA 6409 model was chosen to generate high downforce at low velocities with a zero angle of attack. [2] The cross-section of the spoiler remains constant, as this model is widely used in the automotive sector. The turbulent model adopted for the simulations is the SST k-omega model, which is considered more suitable for a spoiler subjected to a low Reynolds number airflow. [7]

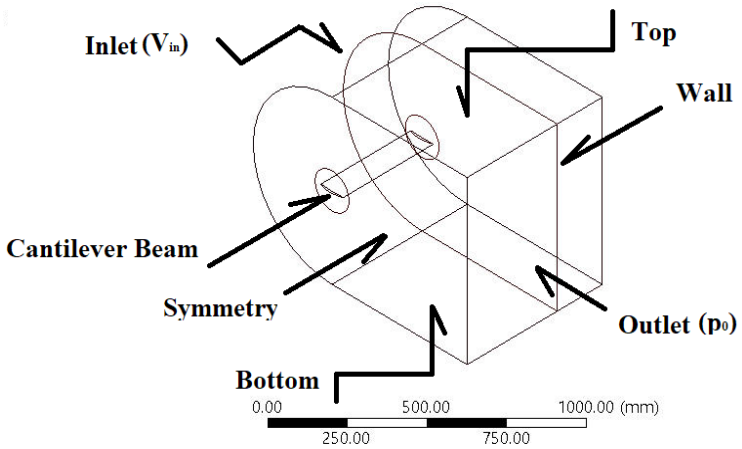

Figure 2: Case study problem geometry with boundary conditions

It was necessary to generate a cylinder around the spoiler to facilitate the change of angle of attack and the automatic and fast regeneration of the mesh.

The inlet velocity of the fluid is variable in the range of 0 to 30 m/s, specifically at 10, 15, 20, 25, and 30 m/s, with an outlet pressure of 0 Pa. The top, bottom, wall, symmetry, and spoiler are set as rigid boundary conditions. The characteristics of the air are as follows: density of 1.175 kg/m³, viscosity of 1.7894×10^{-5} kg/m·s, turbulence intensity of 10%, and incompressible flow with a low Reynolds number.

In the CFD module, a polyhedral mesh composed of cells with 6 sides was used. This type of mesh combines the advantages of 3-sided and 4-sided cells and is obtained by converting a tetrahedral mesh. In other words, the polyhedral mesh, being a hybrid solution, guarantees stability of cell angles with low distortion and provides high convergence speeds. [4]

The minimum orthogonal quality of the polyhedral mesh is 2.97576e-01, and the maximum aspect ratio is 1.45782e+01. In the FEM module, a hexahedral mesh was used. The aspect ratio of the hexahedral mesh is 1.384, and the skewness factor varies from 0.01991 to 0.19302. The Jacobian value of the hexahedral mesh is equal to 1.335 (Fig. 3). [6]

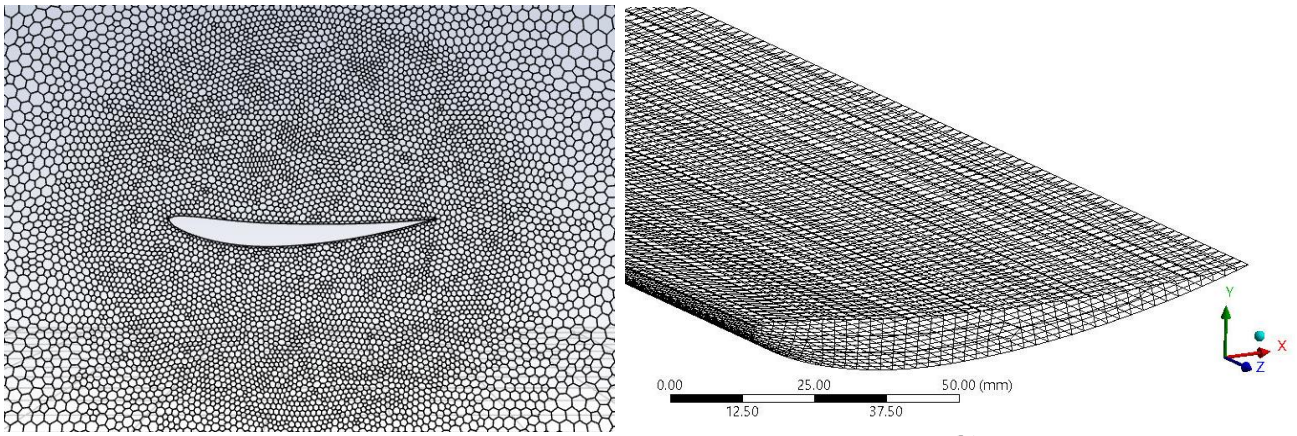

(a) (b)

Figure 3: Zoomed views (a) Polyhedral mesh in CFD domain (b) Hexahedral mesh in FEM domain

A measurement point was selected at a distance of 40 mm from the leading edge of the spoiler to measure the deflections as the velocity, angle of attack, and material type of the spoiler vary. The structural configuration used for the spoiler is that of a cantilever beam, which means one side of the structure is fixed, and the opposite side is free to move. [11]

For laboratory testing, the 3D model was printed using a machine that uses PLA filament. The advantages of PLA filament compared to ABS are that it requires a lower fusion temperature of around 180 ºC, while ABS typically requires a fusion temperature of around 260 ºC. Additionally, PLA does not require a heated print bed like ABS does. However, one disadvantage of PLA is that it has higher viscosity compared to ABS, which can potentially clog the printer nozzle and requires more attention during the printing process. For measuring the deformations of the model in the wind tunnel, a strain gauge with a full bridge configuration was used to amplify the signal and minimize errors caused by temperature variations and resistance in the connecting cables between the sensor and the data acquisition card. Calibration was performed using metallic discs with a mass of 227 grams, which were evenly distributed along the entire surface of the spoiler (fig. 4). [5]

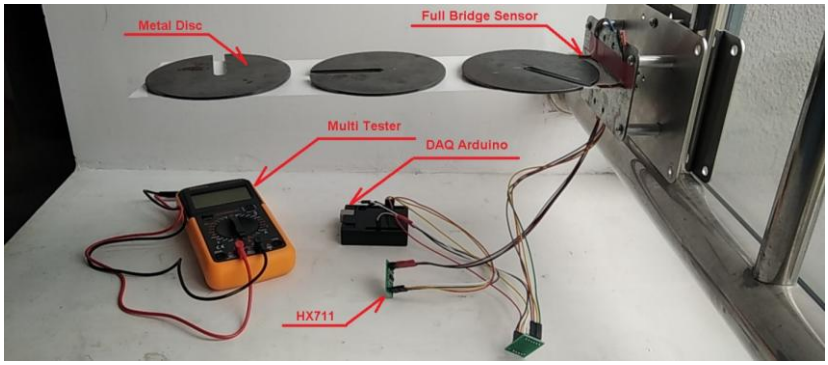

Figure 4: Spoiler deflection under calibration test

The model was tested in an open-type subsonic wind tunnel with a total length of 16.70 meters and a rectangular test section measuring 1.00 x 0.80 x 2.00 meters (fig. 5). The fan that generates the airflow is positioned downstream of the test section and is driven by a three-phase electric motor. The wind tunnel is equipped with various measurement instruments, including static and dynamic pressure sensors, a drag balance, temperature sensors, and humidity sensors. These instruments are connected to a computer controlled by a National Instruments data acquisition card and LabVIEW software for data visualization. [8]

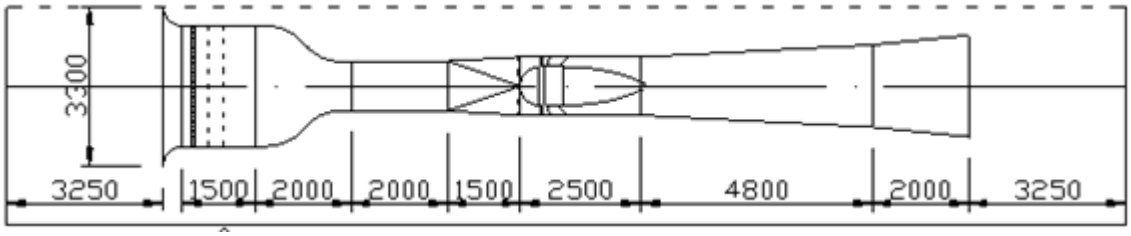

Figure 5: Wind tunnel sheet of Wuhan University of Technology [8]

RESULTS AND DISCUSSION

A parametric analysis was conducted under steady-state conditions for the CFD and FEM modules. The input parameters were the velocity and angle of attack for the CFD, while the output parameter was the deflection of the farthest point from the fixed support of the spoiler for the FEM. The deformations fall within the realm of elasticity and are nonlinear with respect to the airload. Deformations near the fixed support are minimal, while they are maximum at the farthest point.

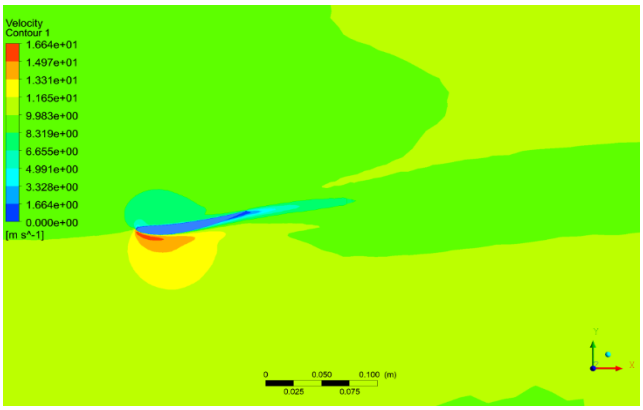

(a)

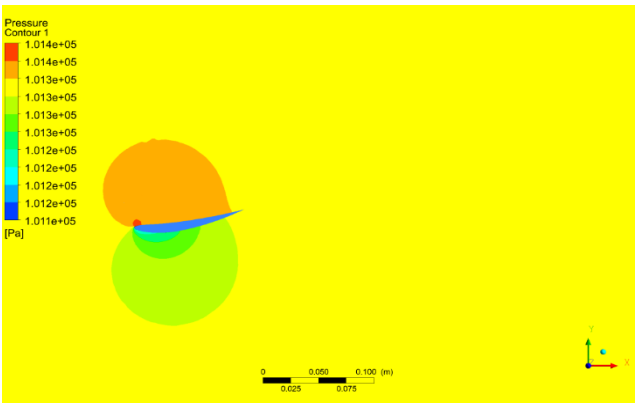

(b)

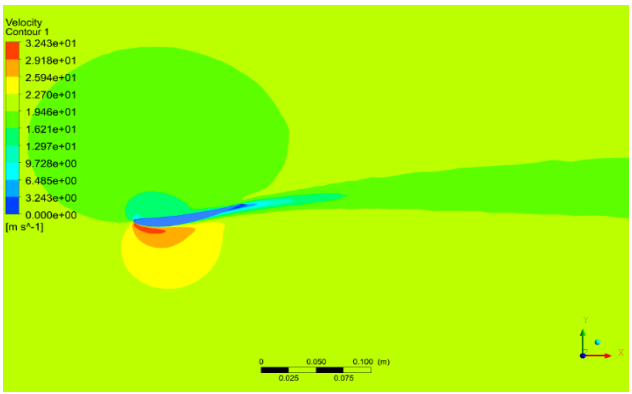

(d)

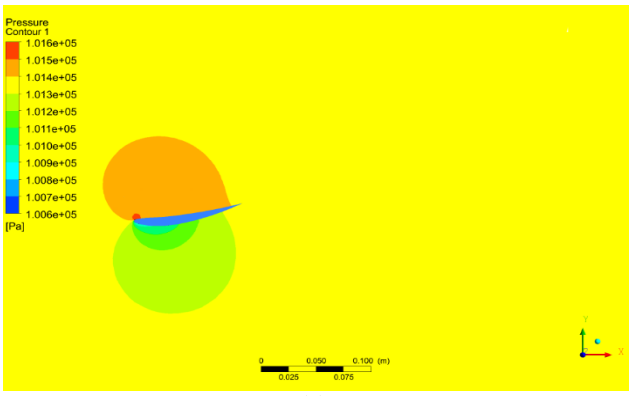

(e)

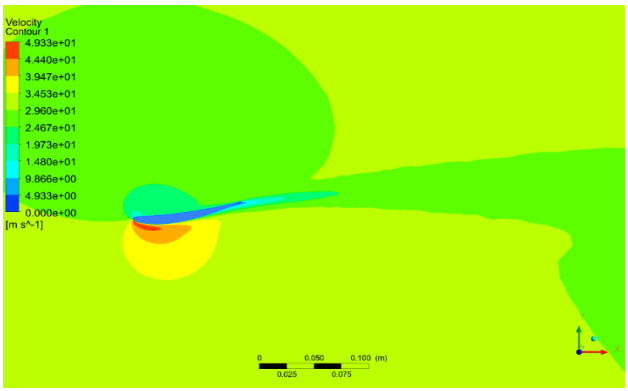

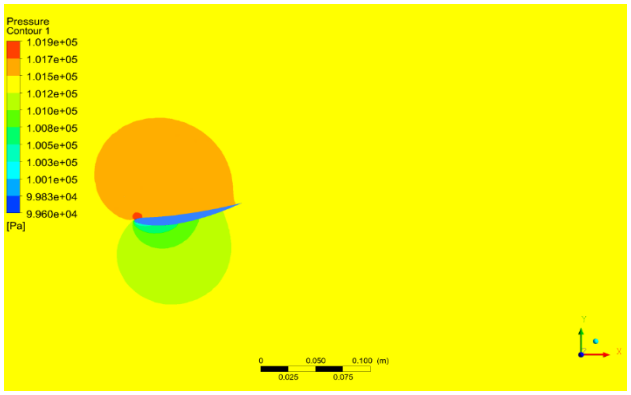

(f) (g)

Figure 4: CFD Contours with 10 degree of AOA (a) Velocity map for Vin 10 m/s (b) Pressure map for Vin 10 m/s (c) Velocity map for Vin 20 m/s (d) Pressure map for Vin 20 m/s (e) Velocity map for Vin 30 m/s (f) Pressure map for Vin 30 m/s

Reynold 66177 – Velocity 10 m/s						
AOA	**Lift Force [N]**	**Drag Force [N]**	**Pitch Mom [J]**	**Lift Coeff.**	**Drag Coeff**	**Pitch. Coeff**
0	-0.887369	0.085748	-0.031078	-0.362192	0.034999	-1.610917
5	-2.043502	0.130794	-0.027316	-0.834082	0.053385	-0.266997
10	-2.305976	0.231579	-0.023555	-0.941214	0.094522	-0.180804
15	-2.469654	0.422243	-0.025471	-1.008022	0.172344	-0.170454
20	-2.423122	0.694051	-0.027387	-0.989029	0.283286	-0.190382
25	-2.392279	1.010170	-0.029459	-0.976440	0.412314	-0.210101
30	-2.438072	1.342334	-0.031531	-0.995131	0.547892	-0.216511
Reynold 132354 – Velocity 20 m/s						
AOA	**Lift Force [N]**	**Drag Force [N]**	**Pitch Mom [J]**	**Lift Coeff.**	**Drag Coeff**	**Pitch. Coeff**
0	-4.402329	0.297546	-0.129562	-0.449217	0.030362	-4.402329
5	-8.584637	0.479256	-0.116442	-0.875983	0.048904	-8.584637
10	-10.368548	0.869497	-0.103323	-1.058015	0.088724	-10.368548
15	-10.529022	1.631611	-0.109515	-1.074390	0.166491	-10.529022
20	-9.999591	2.742778	-0.115707	-1.020366	0.279875	-9.999591
25	-9.668388	4.034571	-0.121821	-0.986570	0.411691	-9.668388
30	-9.813195	5.372940	-0.127934	-1.001346	0.548259	-9.813195
Reynold 198531 – Velocity 30 m/s						
AOA	**Lift Force [N]**	**Drag Force [N]**	**Pitch Mom [J]**	**Lift Coeff.**	**Drag Coeff**	**Pitch. Coeff**
0	-10.509587	0.625479	-0.296879	-0.476625	0.028366	-10.509587
5	-20.099189	1.069499	-0.274840	-0.911528	0.048503	-20.099189
10	-24.556279	1.939251	-0.252801	-1.113663	0.087948	-24.556279
15	-24.538945	3.602681	-0.259523	-1.112877	0.163387	-24.538945
20	-22.777170	6.186906	-0.266245	-1.032978	0.280585	-22.777170
25	-21.995061	9.046215	-0.278081	-0.997508	0.410259	-21.995061
30	-22.148114	12.106269	-0.289917	-1.004450	0.549037	-22.148114

Table 1 Numerical results of Aerodynamics forces and coefficients

Reynold 66177 – Velocity 10 m/s						
AOA	**Lift Force [N]**	**Drag Force [N]**	**Pitch Mom [J]**	**Lift Coeff.**	**Drag Coeff**	**Pitch. Coeff**
0	-0.976105	0.094108	-0.034108	-0.398411	0.038533	-1.783285
5	-2.251939	0.143585	-0.02997	-0.917490	0.058856	-0.293696
10	-2.540032	0.254690	-0.025851	-1.038159	0.103974	-0.359619
15	-2.714149	0.463580	-0.027954	-1.107715	0.189406	-0.187499
20	-2.665434	0.762692	-0.030057	-1.087931	0.314093	-0.209420
25	-2.628396	1.110176	-0.032331	-1.074084	0.454716	-0.417470

30	-2.689193	1.476567	-0.034605	-1.096634	0.602681	-0.237945
Reynold 132354 – Velocity 20 m/s						
AOA	**Lift Force [N]**	**Drag Force [N]**	**Pitch Mom [J]**	**Lift Coeff.**	**Drag Coeff**	**Pitch. Coeff**
0	-4.842562	0.326556	-0.142194	-0.494138	0.033428	-4.873378
5	-9.460269	0.526127	-0.127795	-0.963581	0.053916	-9.443100
10	-11.420955	0.956272	-0.113396	-1.166990	0.097596	-20.623041
15	-11.571395	1.791345	-0.120192	-1.180647	0.182973	-11.581924
20	-10.999550	3.014038	-0.126988	-1.122402	0.310311	-10.999550
25	-10.622657	4.433993	-0.133698	-1.085227	0.454029	-19.211086
30	-10.823954	5.910234	-0.140407	-1.103483	0.603084	-10.784701
Reynold 198531 – Velocity 30 m/s						
AOA	**Lift Force [N]**	**Drag Force [N]**	**Pitch Mom [J]**	**Lift Coeff.**	**Drag Coeff**	**Pitch. Coeff**
0	-11.560545	0.686463	-0.325824	-0.524287	0.031230	-11.634112
5	-22.149306	1.174096	-0.301636	-1.002680	0.053474	-22.109107
10	-27.048741	2.132788	-0.277449	-1.228370	0.096742	-48.842438
15	-26.968300	3.955383	-0.284826	-1.222940	0.179562	-26.992839
20	-25.054887	6.798791	-0.292203	-1.136275	0.311098	-25.054887
25	-24.165973	9.941790	-0.305193	-1.097258	0.452450	-43.704186
30	-24.429369	13.316895	-0.318183	-1.106903	0.603940	-24.340777

Table 2 Measured results of Aerodynamics forces and coefficients

The results of the forces and aerodynamic coefficients developed on the spoiler are presented in Table 1, categorized by Inlet Velocity and Angle of Attack whereas Figure 4 displays typical pressure and velocity maps obtained from the CFD post-processor.

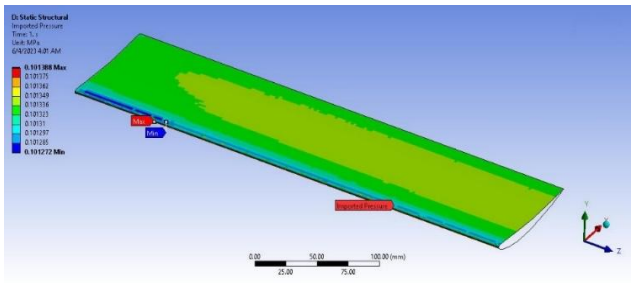

(a)

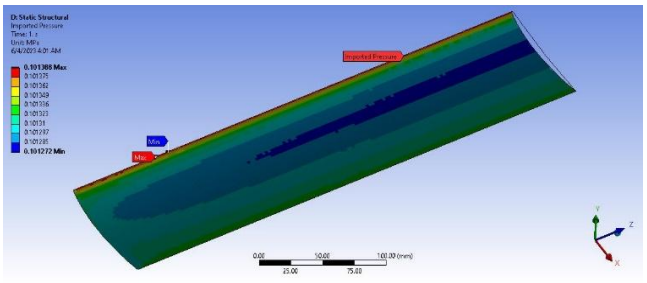

(b)

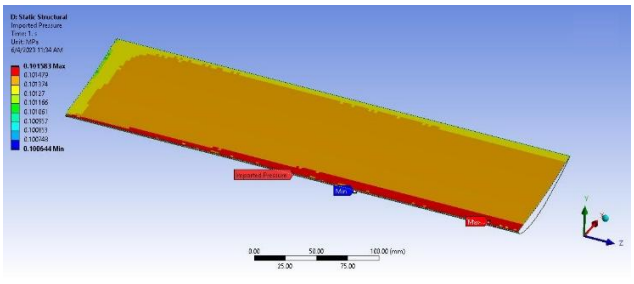

(d)

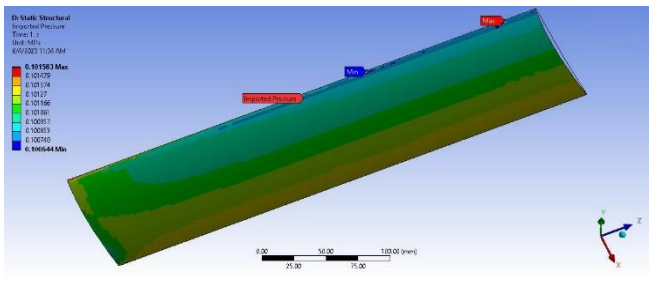

(e)

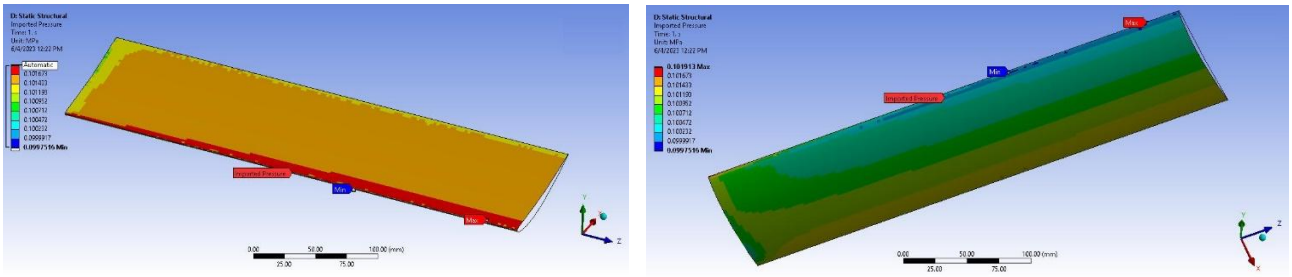

(f) (g)

Figure 5: FEM Contours imported pressure with 10 degree of AOA (a) Top view for Vin 10 m/s (b) Bottom view for Vin 10 m/s (c) Top view for Vin 20 m/s (d) Bottom view for Vin 20 m/s (e) Top view for Vin 30 m/s (f) Bottom view for Vin 30 m/s

In Figure 5, the top and bottom views of the maps of static pressure imported into the FEM module as external pressure are shown. This pressure represents nothing more than the lift force calculated in the CFD module.

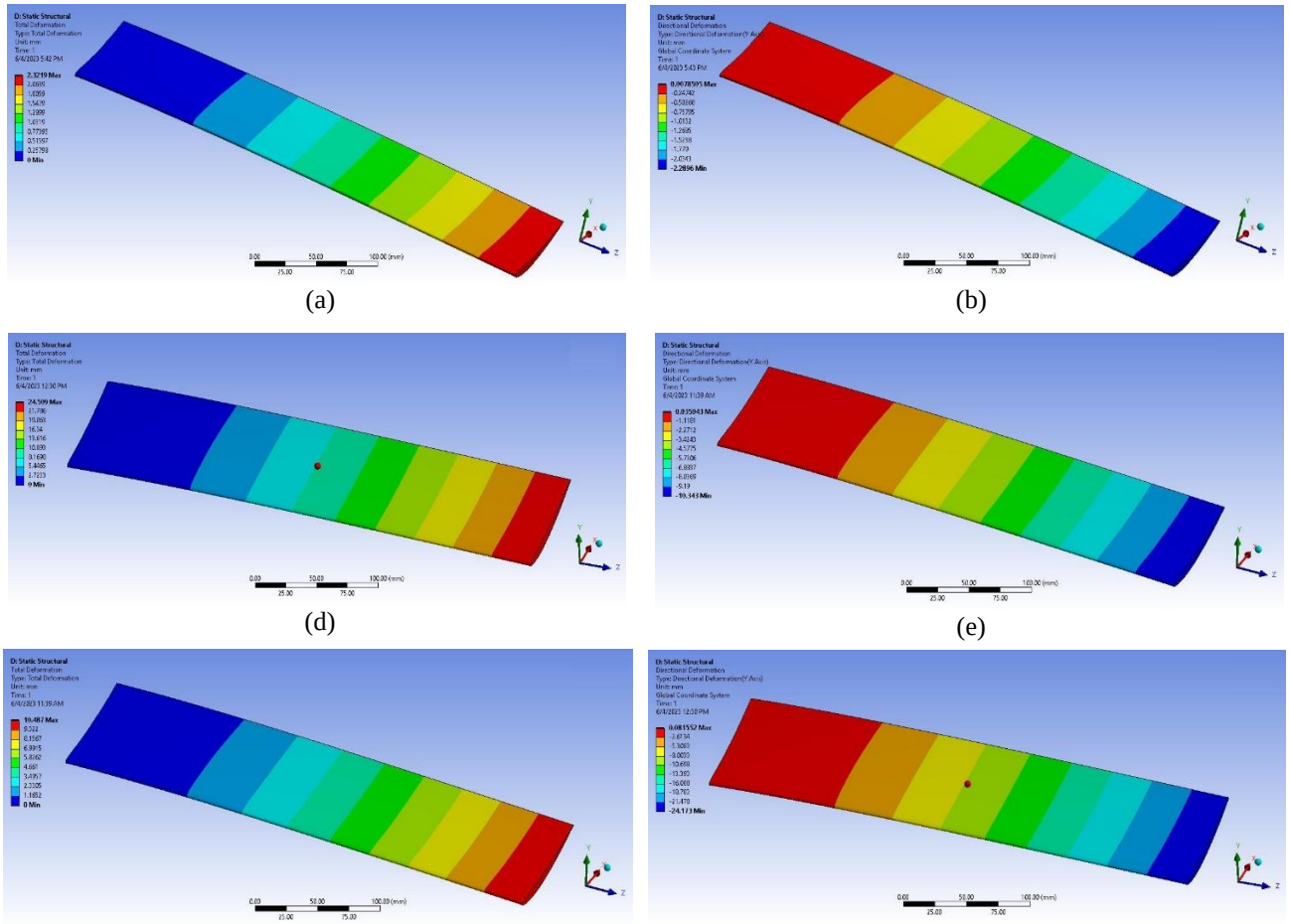

(a) (b)

(d) (e)

(f) (g)

Figure 6: FEM Contours deformations with 10 degree of AOA (a) Total deformation for Vin 10 m/s (b) Directional deformation for Vin 10 m/s (c) Total deformation for Vin 20 m/s (d) Directional deformation for Vin 20 m/s (e) Total deformation for Vin 30 m/s (f) Directional deformation for Vin 30 m/s

Numerical Data					
Velocity [m/s]	**10**	**15**	**20**	**25**	**30**
Y Numerical Displacement @ 0 AOA [mm]	-0.9077	-2.2593	-4.18796	-6.74310	-9.0135
Y Numerical Displacement @ 5 AOA [mm]	-1.7499	-4.0459	-7.3477	-11.8650	-17.2010
Y Numerical Displacement @ 10 AOA [mm]	-1.9339	-4.6767	-8.6826	-13.9770	-20.5550
Y Numerical Displacement @ 15 AOA [mm]	-2.0147	-4.7056	-8.5675	-13.6840	-19.9430
Measured Data					
Velocity [m/s]	**10**	**15**	**20**	**25**	**30**
Y Measured Displacement @ 0 AOA [mm]	-0.9984	-2.4875	-4.6062	-7.4092	-9.9039

Y Measured Displacement @ 5 AOA [mm]	-1.9231	-4.4460	-8.1192	-23.6113	-18.8285
Y Measured Displacement @ 10 AOA [mm]	-3.8426	-5.1603	-9.6194	-27.7806	-22.7215
Y Measured Displacement @ 15 AOA [mm]	-2.2182	-5.1893	-9.4650	-15.0797	-21.9728

Table 3 Total and directional deformation of spoiler

The material used for the spoiler is the typical PLA (Polylactic Acid), with a density of 1240 kg/m^3, Young's modulus of 2210 MPa, tensile yield strength of 26.40 MPa, and tensile ultimate strength of 35.90 MPa. The deformations were calculated relative to the point located in the free section, which is 400 mm away from the fixed support and 40 mm from the leading edge.

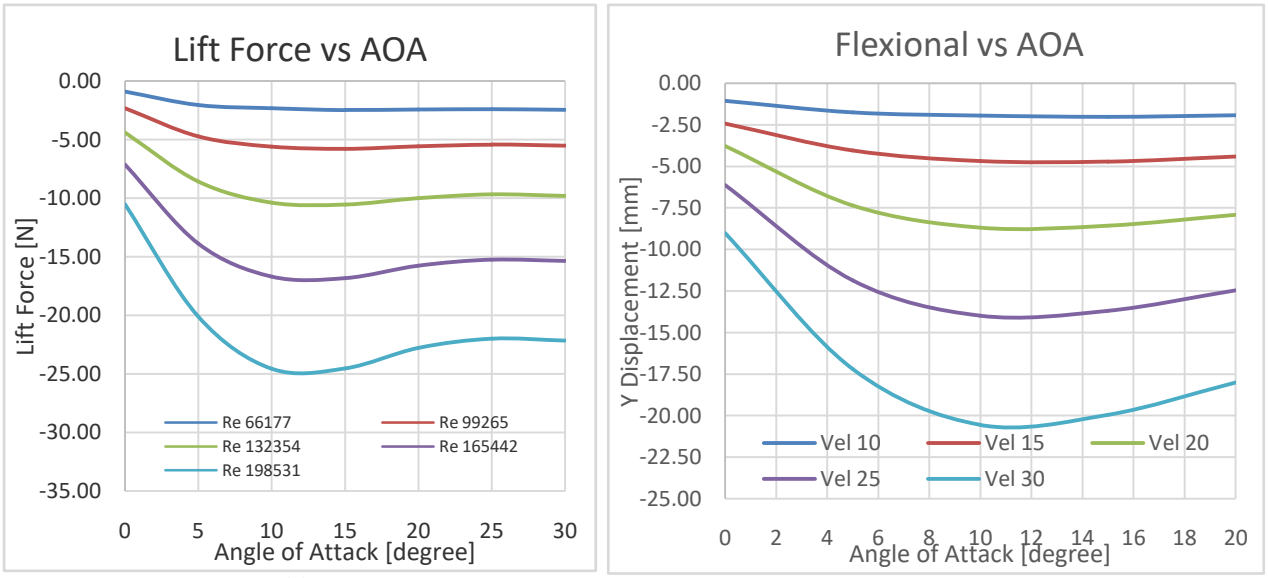

(a) (b)

Figure 7 (a) Lift Force (b) Spoiler Deformation

CONCLUSION

The numerical analysis of the spoiler with an asymmetric airfoil section was performed using the finite volume technique for the CFD domain, and the finite element method for the FEM domain. The analyzed spoiler has a chord length of 10 cm, a span of 40 cm, and a camber of 9%. The mesh used in the CFD environment is polyhedral, while the one used in the FEM environment has a hexahedral geometry. The aerodynamic profile is able to generate high downforce at low speeds, thanks to its camber, with a stall point occurring at 12.5 degrees (fig, 7).

The dominant aerodynamic force is the downforce, which is the negative lift, applied along the upper surface of the spoiler and amounts to $L_\theta = 1/2\rho U^2 S C_{L\theta} = qSC_{L\theta}$. The high aspect ratio of the spoiler minimizes the effect of the moment, which is very low and therefore not considered. The lift force varies between minimum values of -0.887369 N and -2.469654 N for an inlet velocity of 10 m/s, and maximum values of -2.469654 N and -24.556279 N for an inlet velocity of 30 m/s (Tab. 2).

The deformations remain within the elastic range and exhibit a linear relationship with the load, as can be observed from the curves presented in Figure 7a and Figure 7b, which show the same trend.

This analysis highlights that PLA material can be used for the construction of spoilers intended for the automotive sector, particularly for cars that travel on urban and suburban roads where velocities are below 30 m/s. The use of plastic materials for spoiler manufacturing proves to be convenient as it allows for the utilization of fast and efficient 3D printers.

The numerical results deviate from the measured values in the laboratory by approximately 9.8% to 10.2% and the difference appears to be consistent across most cases. It can be concluded that the numerical values are in line with the measured laboratory values and are therefore considered valid since the error between them is relatively low.

REFERENCES

[1]. M. Sathish Kumar, Arun N., S. Jaichandar, (2018). Investigation on Automotive Aerodynamic Drag Reduction of a Hatchback Car by Rear Spoiler usign CFD Analysis. International Journal of Mechanical and Production Engineering Research and Development (IJMPERD), Vol. 8, Issue 2, Apr 2018, 1167-1176
[2]. http://www.airfoiltools.com/
[3]. An Introduction to Aircraft Structural Analysis by T. H. G. Megson, Elsevier Ltd., 2010
[4]. M. Sosnowski, J. Krzywanski, K. Grabowska, R. Gnatowska, Polyhedral meshing in numerical analysis of conjugate heat transfer, The European Physical Journal Conferences, January 2017
[5]. Olsson, Anders, Conceptual Design of Experimental Aircraft (2006)
[6]. Mesh Quality & Advanced Topics of Introduction to ANSYS Meshing
[7]. S. Goyal, A. Kulshreshtha, S. Singh, Selection of Turbulence Model for Analysis of Airfoil Wing using CFD, International Research Journal of Engineering and Technology (IRJET), Volume: 08 Issue: 03, Mar 2021
[8]. Wuhan University of Technology Wind Tunnel
[9]. Elmer S. Hung & Stephan D. Senturia, Generating Efficient Dynamical Models for Microelectromechanical Systems from a Few Finite-Element Simulation Runs, IEEE Journal of Microelectromechanical Systems, Vol. 8, No. 3, pp. 280–289, September 1999.
[10]. Yunus A. Cengel & John M. Cimbala, Differential analysis of fluid flow (Chapter 9). Topics in Fluid Mechaics Fundamentals and Applications, Tata McGraw Hill Education pvt. Ltd., pp. 437–499, 2014.
[11]. L. Huang, Flutter of cantilevered plates in axial flow, Journal of Fluids and Structures, 9, pp. 127–147, 1995.